Accepted by ApJ, January 9^{th} 2011

Detection of a spectral break in the extra hard component of GRB 090926A

M. Ackermann[2], M. Ajello[2], K. Asano[3], M. Axelsson[4,5,6], L. Baldini[7], J. Ballet[8], G. Barbiellini[9,10], M. G. Baring[11], D. Bastieri[12,13], K. Bechtol[2], R. Bellazzini[7], B. Berenji[2], P. N. Bhat[14], E. Bissaldi[15], R. D. Blandford[2], E. Bonamente[16,17], A. W. Borgland[2], A. Bouvier[2], J. Bregeon[7,1], A. Brez[7], M. S. Briggs[14], M. Brigida[18,19], P. Bruel[20], R. Buehler[2], S. Buson[12,13], G. A. Caliandro[21], R. A. Cameron[2], P. A. Caraveo[22], S. Carrigan[13], J. M. Casandjian[8], C. Cecchi[16,17], Ö. Çelik[23,24,25], V. Chaplin[14], E. Charles[2], A. Chekhtman[26,27], J. Chiang[2], S. Ciprini[17], R. Claus[2], J. Cohen-Tanugi[28], V. Connaughton[14], J. Conrad[29,6,30], S. Cutini[31], C. D. Dermer[26], A. de Angelis[32], F. de Palma[18,19], B. L. Dingus[33], E. do Couto e Silva[2], P. S. Drell[2], R. Dubois[2], C. Favuzzi[18,19], S. J. Fegan[20], E. C. Ferrara[23], W. B. Focke[2], M. Frailis[32,34], Y. Fukazawa[35], S. Funk[2], P. Fusco[18,19], F. Gargano[19], D. Gasparrini[31], N. Gehrels[23], S. Germani[16,17], N. Giglietto[18,19], F. Giordano[18,19], M. Giroletti[36], T. Glanzman[2], G. Godfrey[2], A. Goldstein[14,1], J. Granot[37], J. Greiner[15], I. A. Grenier[8], J. E. Grove[26], S. Guiriec[14], D. Hadasch[21], Y. Hanabata[35], A. K. Harding[23], K. Hayashi[35], M. Hayashida[2], E. Hays[23], D. Horan[20], R. E. Hughes[38], R. Itoh[35], G. Jóhannesson[2], A. S. Johnson[2], W. N. Johnson[26], T. Kamae[2], H. Katagiri[35], J. Kataoka[39], R. M. Kippen[33], J. Knödlseder[40], D. Kocevski[2], C. Kouveliotou[41], M. Kuss[7], J. Lande[2], L. Latronico[7], S.-H. Lee[2], M. Llena Garde[29,6], F. Longo[9,10], F. Loparco[18,19], M. N. Lovellette[26], P. Lubrano[16,17], A. Makeev[26,27], M. N. Mazziotta[19], S. McBreen[15,42], J. E. McEnery[23,43], S. McGlynn[44,6], C. Meegan[45], J. Mehault[28], P. Mészáros[46], P. F. Michelson[2], T. Mizuno[35], C. Monte[18,19], M. E. Monzani[2], E. Moretti[44,6], A. Morselli[47], I. V. Moskalenko[2], S. Murgia[2], H. Nakajima[48], T. Nakamori[39], M. Naumann-Godo[8], S. Nishino[35], P. L. Nolan[2], J. P. Norris[49], E. Nuss[28], M. Ohno[50], T. Ohsugi[51], A. Okumura[50], N. Omodei[2], E. Orlando[15], J. F. Ormes[49], M. Ozaki[50], W. S. Paciesas[14], D. Paneque[2], J. H. Panetta[2], D. Parent[26,27], V. Pelassa[28], M. Pepe[16,17], M. Pesce-Rollins[7], V. Petrosian[2], F. Piron[28], T. A. Porter[2], R. Preece[14,1], J. L. Racusin[23], S. Rainò[18,19], R. Rando[12,13], A. Rau[15], M. Razzano[7], S. Razzaque[26,52], A. Reimer[53,2], O. Reimer[53,2], T. Reposeur[54], L. C. Reyes[55], J. Ripken[29,6], S. Ritz[56], M. Roth[57], F. Ryde[44,6], H. F.-W. Sadrozinski[56], A. Sander[38], J. D. Scargle[58], T. L. Schalk[56], C. Sgrò[7], E. J. Siskind[59], P. D. Smith[38], G. Spandre[7], P. Spinelli[18,19], M. Stamatikos[23,38], F. W. Stecker[23], M. S. Strickman[26], D. J. Suson[60], H. Tajima[2], H. Takahashi[51,1], T. Tanaka[2], Y. Tanaka[50], J. B. Thayer[2], J. G. Thayer[2], L. Tibaldo[12,13,8,61], D. Tierney[42], K. Toma[46,1], D. F. Torres[21,62], G. Tosti[16,17], A. Tramacere[2,63,64], Y. Uchiyama[2], T. Uehara[35,1], T. L. Usher[2], J. Vandenbroucke[2], A. J. van der Horst[41,65], V. Vasileiou[24,25],

N. Vilchez[40], V. Vitale[47,66], A. von Kienlin[15], A. P. Waite[2], P. Wang[2], C. Wilson-Hodge[41], B. L. Winer[38], K. S. Wood[26], X. F. Wu[46,67,68], R. Yamazaki[69], Z. Yang[29,6], T. Ylinen[44,70,6], M. Ziegler[56]

[1]Corresponding authors: J. Bregeon, johan.bregeon@pi.infn.it; A. Goldstein, amg0005@uah.edu; R. Preece, Rob.Preece@nasa.gov; H. Takahashi, hirotaka@hep01.hepl.hiroshima-u.ac.jp; K. Toma, toma@astro.psu.edu; T. Uehara, uehara@hep01.hepl.hiroshima-u.ac.jp.

[2]W. W. Hansen Experimental Physics Laboratory, Kavli Institute for Particle Astrophysics and Cosmology, Department of Physics and SLAC National Accelerator Laboratory, Stanford University, Stanford, CA 94305, USA

[3]Interactive Research Center of Science, Tokyo Institute of Technology, Meguro City, Tokyo 152-8551, Japan

[4]Department of Astronomy, Stockholm University, SE-106 91 Stockholm, Sweden

[5]Lund Observatory, SE-221 00 Lund, Sweden

[6]The Oskar Klein Centre for Cosmoparticle Physics, AlbaNova, SE-106 91 Stockholm, Sweden

[7]Istituto Nazionale di Fisica Nucleare, Sezione di Pisa, I-56127 Pisa, Italy

[8]Laboratoire AIM, CEA-IRFU/CNRS/Université Paris Diderot, Service d'Astrophysique, CEA Saclay, 91191 Gif sur Yvette, France

[9]Istituto Nazionale di Fisica Nucleare, Sezione di Trieste, I-34127 Trieste, Italy

[10]Dipartimento di Fisica, Università di Trieste, I-34127 Trieste, Italy

[11]Rice University, Department of Physics and Astronomy, MS-108, P. O. Box 1892, Houston, TX 77251, USA

[12]Istituto Nazionale di Fisica Nucleare, Sezione di Padova, I-35131 Padova, Italy

[13]Dipartimento di Fisica "G. Galilei", Università di Padova, I-35131 Padova, Italy

[14]Center for Space Plasma and Aeronomic Research (CSPAR), University of Alabama in Huntsville, Huntsville, AL 35899, USA

[15]Max-Planck Institut für extraterrestrische Physik, 85748 Garching, Germany

[16]Istituto Nazionale di Fisica Nucleare, Sezione di Perugia, I-06123 Perugia, Italy

[17]Dipartimento di Fisica, Università degli Studi di Perugia, I-06123 Perugia, Italy

[18]Dipartimento di Fisica "M. Merlin" dell'Università e del Politecnico di Bari, I-70126 Bari, Italy

[19]Istituto Nazionale di Fisica Nucleare, Sezione di Bari, 70126 Bari, Italy

[20]Laboratoire Leprince-Ringuet, École polytechnique, CNRS/IN2P3, Palaiseau, France

[21]Institut de Ciencies de l'Espai (IEEC-CSIC), Campus UAB, 08193 Barcelona, Spain

[22]INAF-Istituto di Astrofisica Spaziale e Fisica Cosmica, I-20133 Milano, Italy

[23]NASA Goddard Space Flight Center, Greenbelt, MD 20771, USA

[24]Center for Research and Exploration in Space Science and Technology (CRESST) and NASA Goddard

Space Flight Center, Greenbelt, MD 20771, USA

[25]Department of Physics and Center for Space Sciences and Technology, University of Maryland Baltimore County, Baltimore, MD 21250, USA

[26]Space Science Division, Naval Research Laboratory, Washington, DC 20375, USA

[27]George Mason University, Fairfax, VA 22030, USA

[28]Laboratoire de Physique Théorique et Astroparticules, Université Montpellier 2, CNRS/IN2P3, Montpellier, France

[29]Department of Physics, Stockholm University, AlbaNova, SE-106 91 Stockholm, Sweden

[30]Royal Swedish Academy of Sciences Research Fellow, funded by a grant from the K. A. Wallenberg Foundation

[31]Agenzia Spaziale Italiana (ASI) Science Data Center, I-00044 Frascati (Roma), Italy

[32]Dipartimento di Fisica, Università di Udine and Istituto Nazionale di Fisica Nucleare, Sezione di Trieste, Gruppo Collegato di Udine, I-33100 Udine, Italy

[33]Los Alamos National Laboratory, Los Alamos, NM 87545, USA

[34]Osservatorio Astronomico di Trieste, Istituto Nazionale di Astrofisica, I-34143 Trieste, Italy

[35]Department of Physical Sciences, Hiroshima University, Higashi-Hiroshima, Hiroshima 739-8526, Japan

[36]INAF Istituto di Radioastronomia, 40129 Bologna, Italy

[37]Centre for Astrophysics Research, Science and Technology Research Institute, University of Hertfordshire, Hatfield AL10 9AB, UK

[38]Department of Physics, Center for Cosmology and Astro-Particle Physics, The Ohio State University, Columbus, OH 43210, USA

[39]Research Institute for Science and Engineering, Waseda University, 3-4-1, Okubo, Shinjuku, Tokyo, 169-8555 Japan

[40]Centre d'Étude Spatiale des Rayonnements, CNRS/UPS, BP 44346, F-30128 Toulouse Cedex 4, France

[41]NASA Marshall Space Flight Center, Huntsville, AL 35812, USA

[42]University College Dublin, Belfield, Dublin 4, Ireland

[43]Department of Physics and Department of Astronomy, University of Maryland, College Park, MD 20742, USA

[44]Department of Physics, Royal Institute of Technology (KTH), AlbaNova, SE-106 91 Stockholm, Sweden

[45]Universities Space Research Association (USRA), Columbia, MD 21044, USA

[46]Department of Astronomy and Astrophysics, Pennsylvania State University, University Park, PA 16802, USA

[47]Istituto Nazionale di Fisica Nucleare, Sezione di Roma "Tor Vergata", I-00133 Roma, Italy

ABSTRACT

We report on the observation of the bright, long gamma-ray burst, GRB 090926A, by the Gamma-ray Burst Monitor (GBM) and Large Area Tele-

[48]Department of Physics, Tokyo Institute of Technology, Meguro City, Tokyo 152-8551, Japan

[49]Department of Physics and Astronomy, University of Denver, Denver, CO 80208, USA

[50]Institute of Space and Astronautical Science, JAXA, 3-1-1 Yoshinodai, Sagamihara, Kanagawa 229-8510, Japan

[51]Hiroshima Astrophysical Science Center, Hiroshima University, Higashi-Hiroshima, Hiroshima 739-8526, Japan

[52]National Research Council Research Associate, National Academy of Sciences, Washington, DC 20001, USA

[53]Institut für Astro- und Teilchenphysik and Institut für Theoretische Physik, Leopold-Franzens-Universität Innsbruck, A-6020 Innsbruck, Austria

[54]Université Bordeaux 1, CNRS/IN2p3, Centre d'Études Nucléaires de Bordeaux Gradignan, 33175 Gradignan, France

[55]Kavli Institute for Cosmological Physics, University of Chicago, Chicago, IL 60637, USA

[56]Santa Cruz Institute for Particle Physics, Department of Physics and Department of Astronomy and Astrophysics, University of California at Santa Cruz, Santa Cruz, CA 95064, USA

[57]Department of Physics, University of Washington, Seattle, WA 98195-1560, USA

[58]Space Sciences Division, NASA Ames Research Center, Moffett Field, CA 94035-1000, USA

[59]NYCB Real-Time Computing Inc., Lattingtown, NY 11560-1025, USA

[60]Department of Chemistry and Physics, Purdue University Calumet, Hammond, IN 46323-2094, USA

[61]Partially supported by the International Doctorate on Astroparticle Physics (IDAPP) program

[62]Institució Catalana de Recerca i Estudis Avançats (ICREA), Barcelona, Spain

[63]Consorzio Interuniversitario per la Fisica Spaziale (CIFS), I-10133 Torino, Italy

[64]INTEGRAL Science Data Centre, CH-1290 Versoix, Switzerland

[65]NASA Postdoctoral Program Fellow, USA

[66]Dipartimento di Fisica, Università di Roma "Tor Vergata", I-00133 Roma, Italy

[67]Joint Center for Particle Nuclear Physics and Cosmology (J-CPNPC), Nanjing 210093, China

[68]Purple Mountain Observatory, Chinese Academy of Sciences, Nanjing 210008, China

[69]Aoyama Gakuin University, Sagamihara-shi, Kanagawa 229-8558, Japan

[70]School of Pure and Applied Natural Sciences, University of Kalmar, SE-391 82 Kalmar, Sweden

scope (LAT) instruments on board the *Fermi* Gamma-ray Space Telescope. GRB 090926A shares several features with other bright LAT bursts. In particular, it clearly shows a short spike in the light curve that is present in all detectors that see the burst, and this in turn suggests that there is a common region of emission across the entire *Fermi* energy range. In addition, while a separate high-energy power-law component has already been observed in other GRBs, here we report for the first time the detection with good significance of a high-energy spectral break (or cutoff) in this power-law component around 1.4 GeV in the time-integrated spectrum. If the spectral break is caused by opacity to electron-positron pair production within the source, then this observation allows us to compute the bulk Lorentz factor for the outflow, rather than a lower limit.

Subject headings: gamma rays: bursts

1. Introduction

Gamma-Ray Bursts (GRBs) are the most energetic transients in the universe. The first brief and intense flash, the so-called prompt emission, has been observed in the X-ray and gamma-ray bands, while subsequent long-lived afterglow emission has so far been observed mainly at energies in the X-ray band and below. The prompt emission is thought to be produced in an ultra-relativistic outflow, but its detailed emission mechanism has been a long-standing problem. It has been widely believed that the afterglow is the synchrotron emission from the forward shock that propagates in the external medium, but *Swift* observations have pointed out some difficulties in this model (for recent reviews, Zhang 2007; Mészáros 2006). The study of the gamma-ray emission in the GeV energy range is expected to give us important information on these issues and even on the nature of the progenitors and the ultra-relativistic outflows of GRBs (Band et al. 2009; Falcone et al. 2008; Fan & Piran 2008).

The *Fermi* Gamma-ray Space Telescope hosts two instruments, the Large Area Telescope (LAT, 20 MeV to more than 300 GeV; Atwood et al. 2009) and the Gamma-ray Burst Monitor (GBM, 8 keV–40 MeV; Meegan et al. 2009), which together are capable of measuring the spectral parameters of GRBs across seven decades in energy. Since the start of science operations in early August 2008, the *Fermi* LAT has significantly detected 16 GRBs. These events, including the very bright long-duration and short-duration bursts GRB 080825C, GRB 080916C, GRB 081024B, GRB 090510, and GRB 090902B, have revealed many important, seemingly common, features of GRB GeV emission (Abdo et al. 2009a,b,c,d, 2010;

Ackermann et al. 2010a,b): (1) the GeV emission onsets of many LAT GRBs are delayed with respect to the MeV emission onsets; (2) some LAT GRBs have extra hard components apart from the canonical Band function (Band et al. 1993), which typically peaks in νF_ν between around 100 keV–1 MeV; (3) the GeV emission lasts longer than the prompt MeV emission, showing power-law temporal decays at late times.

In this paper, we report on the analysis of the bright, long GRB 090926A detected by *Fermi* LAT/GBM. The light curve of this burst above 100 MeV shows a sharp spike with a width of 0.15 s, fast variability that we use to constrain the origin of the high-energy photons within the spike. Furthermore, from the detection of a break in the >100 MeV gamma-ray spectrum, we derive constraints on the bulk Lorentz factor and the distance of the emitting region from the central source. Section 2 summarizes the detections of GRB 090926A by the GBM and the LAT, and the follow-up observations. Section 3 presents the light curves of the prompt emission as seen by both instruments and describes a sharp pulse seen in all detectors. In section 4, we detail the spectral analysis of the burst through time-resolved spectroscopy, the measurement of a break in the extra-component, and the extended emission found in the LAT data out to 4.8 ks after the trigger. These last two points are at the center of the physical interpretation of the observations that is developed in section 5.1. Throughout this paper, we adopt a Hubble constant of $H_0 = 72$ km s^{-1} Mpc^{-1} and cosmological parameters of $\Omega_\Lambda = 0.73$ and $\Omega_M = 0.27$.

2. Observations

At 04:20:26.99 (UT) on Sept. 26, 2009 (hereafter $T_0 = 275631628.98$ s mission elapsed time), the *Fermi* Gamma-ray Burst Monitor (GBM) triggered on and localized the long GRB 090926A at (RA, Dec) = (354.5°, −64.2°), in J2000 coordinates (Bissaldi 2009; Uehara et al. 2009). This position was ∼52° with respect to the LAT boresight at the time of the trigger and well within the field of view. An Autonomous Repoint Request (ARR) was generated, but the spacecraft initially remained in survey mode as the Earth avoidance angle condition was not satisfied by the burst pointing direction. The on-board GBM position of GRB 090926A was occulted by the Earth at roughly $T_0 + 500$ s until it rose above the horizon at approximately $T_0 + 3000$ s. At that time, the spacecraft slewed to GRB 090926A and kept it close to the center of the LAT field of view until $T_0 + 18000$ s, though the source location was occulted by the Earth several times over that time period.

Emission from GRB 090926A was evident in the *Fermi* LAT raw trigger event rates, and the number of LAT events (~ 200 photon candidates above 100 MeV) is comparable to that of the other bright LAT bursts, GRB 080916C, GRB 090510 and GRB 090902B. The increase

in the photon count rate during the prompt phase is spatially and temporally correlated with the GBM emission with high significance, and extended emission is observed until $T_0 + 4800$ s. The best LAT on-ground localization is (RA, Dec) = (353.56°, −66.34°), with a 90% containment radius of 0.07° (statistical; 68% containment radius: 0.04°, systematic error is less than 0.1°) and is consistent with the XRT localization.

Indeed, based upon the GCN report issued for the LAT detection, a *Swift* TOO observation was performed, and an afterglow for GRB 090926A was detected with XRT and UVOT at $T_0 + 47$ ks and localized at (RA, Dec) = (353.40070°, -66.32390°) with an uncertainty of 1.5 ″(90% confidence) (Vetere et al. 2009). VLT observations determined a redshift for GRB 090926A of $z = 2.1062$, using the X-shooter spectrograph (Malesani et al. 2009). Suzaku/WAM and Skynet/PROMPT also detected the soft gamma-ray prompt and optical afterglow emission, respectively (Noda et al. 2009).

3. Light Curves

In figure 1, we show the GBM and LAT light curves in several energy bands. The highest energy photon is a 19.6 GeV event, observed at $T_0 + 25$ s within 0.03° from the LAT position of GRB 090926A, well within the 68% containment of the point spread function at that energy. The light curves show that the onset of the LAT emission is delayed by 3.3 s with respect to the GBM emission, similar to other LAT GRBs (Abdo et al. 2009a,b,c,d, 2010; Ackermann et al. 2010a,b). Detailed analysis of the GBM data results in a formal T90 duration[1] (Kouveliotou et al. 1993) of 13.1 ± 0.2 s, with a start time of $T_0 + 2.2$ s and a stop time of $T_0 + 15.3$ s. The emission measured in the LAT above 100 MeV has a similar duration; however, owing to the efficient background rejection applied to the LAT data, the signal is clearly visible in the light curve well after this time range.

The time intervals chosen for spectroscopy are indicated by the vertical lines in figure 1, with boundaries at $T_0 + (0, 3.3, 9.8, 10.5, 21.6)$ s. The end of the last time interval at $T_0 + 21.6$ s was chosen somewhat arbitrarily as the end of the prompt phase, but we carefully verified that our results are not affected by a slightly different choice. Figure 2 shows a zoom of some of the light curves between $T_0 + 2.2$ s and $T_0 + 15.3$ s, with a binning of 0.05 s, and highlights the presence of the sharp peak seen in each of the NaI, BGO, and LAT light curves at $T_0 + 10$ s. As seen on figure 2, the peak is clearly in coincidence in all of the light curves, indicating a strong correlation of the emission from a few keV to energies > 100

[1]The T90 duration is the time over which the central 90% of the counts between 50 and 300 keV have been accumulated.

MeV. Because this peak is the only one evident at all energies, we chose to run a dedicated spectral analysis between $T_0 + 9.8\,\mathrm{s}$ and $T_0 + 10.5\,\mathrm{s}$ as described in section 4.1.

We estimated the variability time scale using the full width at half maximum (FWHM) of the bright pulse seen around $T_0 + 10\,\mathrm{s}$. A combination of exponential functions is used to fit the light curve as performed in Norris et al. (1996). The light curve fitting is performed for all bright NaI detectors (N6, N7, N8) with a 2 ms time resolution. Two exponential functions are used to represent the weak and main bright peaks and include a quadratic function to fit the longer timescale variations. As a result, we obtain a FWHM of the main peak of $0.15 \pm 0.01\,\mathrm{s}$ for the bright pulse.

4. Spectral Analysis

4.1. LAT and GBM spectral fitting

We performed a time-integrated joint spectral analysis of the LAT and GBM data for the prompt phase defined as $T_0 + 3.3\,\mathrm{s}$ to $T_0 + 21.6\,\mathrm{s}$ in figure 1. For the GBM, we used 'Time Tagged Events' (TTE) data from the NaI detectors 6, 7, 8 and BGO detector 1. As in Abdo et al. (2009d), background rates and errors are estimated during the prompt phase by fitting background regions of the light curve before and after the burst. We derived our background estimates using the time intervals $[T_0 - 44; T_0 - 8]\,\mathrm{s}$ and $[T_0 + 36; T_0 + 100]\,\mathrm{s}$ for the NaI detectors, and $[T_0 - 43; T_0 - 16]\,\mathrm{s}$ and $[T_0 + 43; T_0 + 300]\,\mathrm{s}$ for the BGO detector. For the LAT, we extracted 'transient' class data from an energy-dependent acceptance cone around the burst position, as described in Abdo et al. (2009d), and considered front- and back-converting events separately (Atwood et al. 2009). The data files for the analysis were prepared using the LAT `ScienceTools-v9r15p2` package, which is available from the *Fermi* Science Support Center (FSSC), and the `P6_V3_TRANIENT` response functions.[71] A synthetic background was derived for the LAT data using an empirical model of the rates expected for the position of the source in the sky and for the position and orientation of the spacecraft during the burst interval.

The joint spectral fitting of GBM and LAT data was performed using *rmfit* version 3.2 (Kaneko et al. 2006; Abdo et al. 2009d), which estimates the goodness-of-fit in terms of the Castor Statistic (C-STAT) to handle correctly the small number of events at the highest energies. The Castor statistic (Dorman 2003) is similar to the Cash statistic (Cash 1979) except for an offset that is constant for a particular dataset. A global effective area correction

[71] `http://fermi.gsfc.nasa.gov/ssc/`

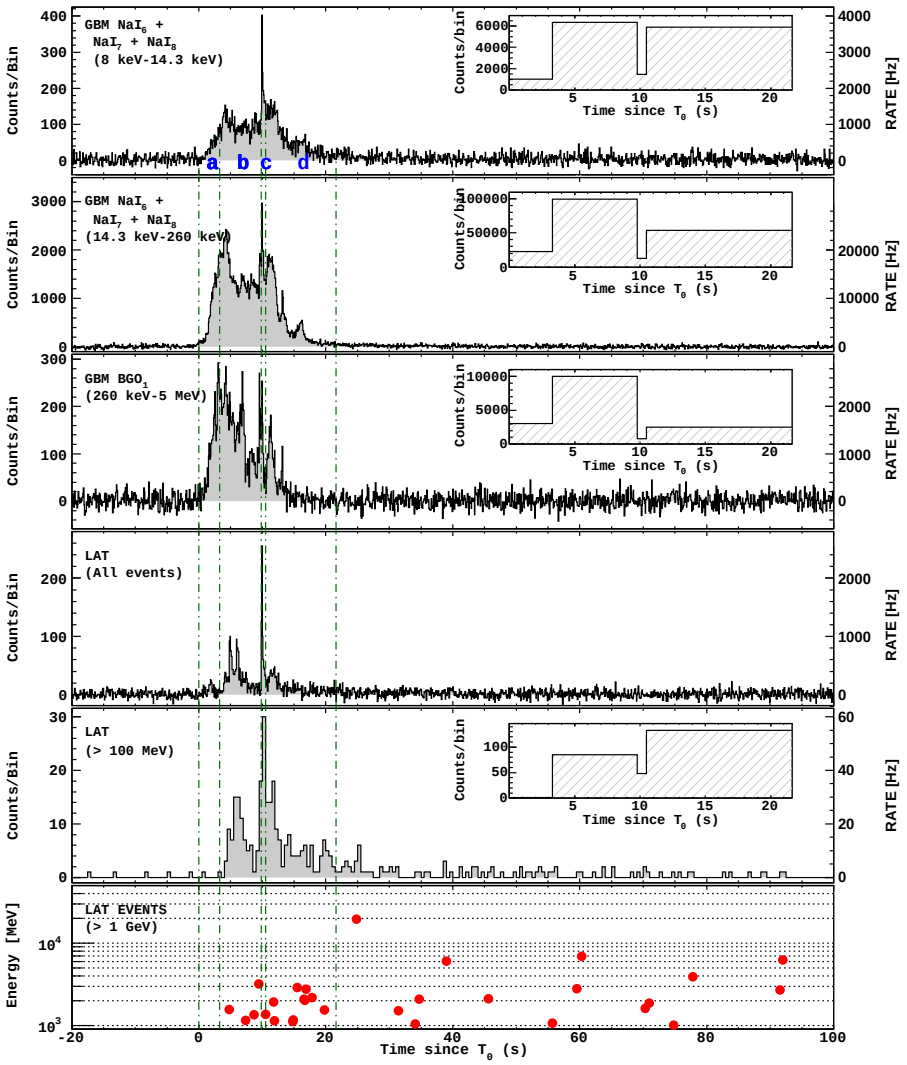

Fig. 1.— GBM and LAT light curves for the gamma-ray emission of GRB 090926A. The data from the GBM NaI detectors were divided into soft (8–14.3 keV) and hard (14.3–260 keV) bands to reveal similarities between the light curve at the lowest energies and that of the LAT data. The fourth panel shows all LAT events that pass the on-board GAMMA filter (Atwood et al. 2009). The first four light curves are background-subtracted and are shown for 0.1 s time bins. The fifth and sixth panels show LAT data 'transient' class events for energies > 100 MeV and > 1 GeV respectively, both using 0.5 s time bins. The vertical lines indicate the boundaries of the intervals used for the time-resolved spectral analysis, $T_0 + (0, 3.3, 9.8, 10.5, 21.6)$ s. The insets show the counts for each data set, binned using these intervals, to illustrate the numbers of counts considered in each spectral fit.

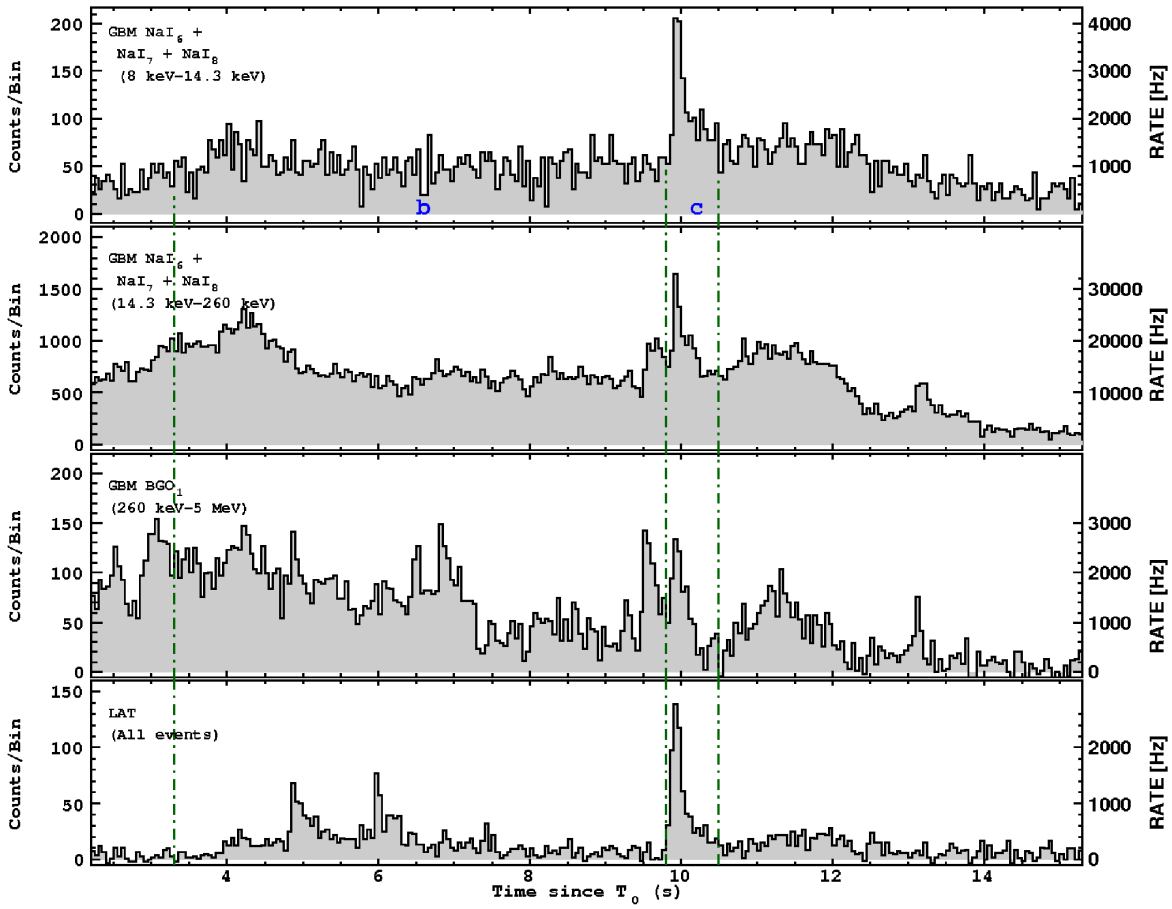

Fig. 2.— GBM and LAT light curves for the gamma-ray emission of GRB 090926A with 0.05 s time binning for the core of the prompt phase. The vertical dashed lines at $T_0 + 9.8$ s and $T_0 + 10.5$ s define interval c used in the spectral analysis, see section 4.1.

has been applied to the BGO data to match the model normalizations given by the NaI data; this correction is consistent with the relative uncertainties in the GBM detector responses. Uncorrected, this will normally cause a mismatch between the fitted model rates between the two types of detectors where they overlap in energy. Once the correction has been determined, it is held fixed throughout the calculation, since it reflects an uncertainty in the response rather than in the data. In this analysis, the NaI to BGO normalization factor was found to be 0.79. For further details on the data extraction and spectral analysis procedures see our previous publications Abdo et al. (2009d) and Abdo et al. (2010).

Initially, we fitted a canonical Band function (Band et al. 1993) to the data and then found that adding an extra power-law component improved both the fit statistics and residuals. Table 1 summarizes the best-fit parameters and shows that the improvement in C-STAT for the (Band+PL) fit over the Band fit alone is 107.3, indicating a firm detection of the additional power-law component. The parameters of the Band function are stable, and the power-law photon index of the additional component is $\lambda = -1.79 \pm 0.02$.

In order to better characterize the power-law component at the highest energies, we ran a LAT-only data analysis using the unbinned likelihood technique for the full prompt phase. The fitted spectrum is shown in figure 3 (black points). The resulting photon index is -2.29 ± 0.09, much softer than the -1.79 ± 0.02 index found for the joint GBM/LAT analysis. Considering the systematic effects in both analyses, this difference in photon index is significant ($\sim 3\sigma$ level) and is an indication of the presence of a spectral break. With the LAT data alone, we could not find any significant evidence for a deviation from the simple power-law shape, probably because of the limited lever arm in energy. Hence, we investigated this effect using the joint fits of the GBM and LAT data.

We fitted the GBM/LAT spectra with the combination of the Band function and a power-law model with an exponential cutoff (CUTPL),

$$f(E) = B \left(\frac{E}{E_{\rm piv}} \right)^{\lambda} \exp \left(-\frac{E}{E_F} \right). \quad (1)$$

Here B is the normalization in units of photons $\rm s^{-1}$ $\rm cm^{-2}$ $\rm keV^{-1}$, $E_{\rm piv}$ is the pivot energy fixed at 1 GeV, E_F is the e-folding energy, and λ is the power-law photon index.

The fit results are summarized in table 1, and the count spectra and residuals are shown in figure 4 for the best-fit model. The e-folding energy is $E_F = 1.41^{+0.22}_{-0.42}$ *stat.* $\pm$ 0.30 *syst.* GeV, while the power-law photon index below the cutoff energy is $\lambda \simeq -1.72^{+0.10}_{-0.02}$ *stat.* $\pm$ 0.01 *syst.*, which is a bit harder than in the (Band+PL) case. The systematic uncertainties have been derived using the bracketing instrument response functions, as described in detail in Abdo et al. (2009d). The parameters of the Band function change little from one fit to

another. The C-STAT value for this model improves by 40.5 compared to the (Band+PL) model, which is significant at the $> 4\sigma$ level (see the deeper discussion below). We also tried to fit the data with a broken power-law model,

$$f(E) \;=\; \left\{ \begin{array}{lll} C\left(\frac{E}{E_{\rm piv}}\right)^{\lambda_l} & & \text{for } E \le E_{\rm break} \\ C\left(\frac{E_{\rm break}}{E_{\rm piv}}\right)^{\lambda_l} & \left(\frac{E}{E_{\rm break}}\right)^{\lambda_h} & \text{for } E > E_{\rm break} \end{array} \right\}, \qquad (2)$$

where λ_l and λ_h are the low- and high-energy power-law photon indexes, respectively, $E_{\rm piv}$ is the pivot energy fixed at 1 GeV, and $E_{\rm break}$ is the break energy. However, the significance of the fit was close to that found using the (CUTPL) model so that we cannot distinguish between the two models. The fit with a broken power-law gave a break energy $E_{\rm break} = 219^{+65}_{-56}$ MeV and a high-energy photon index of $\lambda_h = -2.47^{+0.14}_{-0.17}$.

One may assess the significance of the spectral cutoff by computing the difference in the best-fit C-STAT values for the (Band+PL) and (Band+CUTPL) models. Since C-STAT is equal to twice the log-likelihood, this is the standard likelihood ratio test; and conventionally, one calculates the significance of a change in log-likelihood using Wilks' theorem. In this case, Wilks' theorem states the Δ(C-STAT) values should be asymptotically distributed as χ^2 for one degree of freedom. However, certain assumptions are required for the validity of this calculation. For the highest reliability, we studied the distribution of Δ(C-STAT) values via simulations, creating 2×10^4 random realizations of the null hypothesis (the (Band+PL) model with parameters set at the best-fit values) and fit the data for each trial with both models. In the resulting distribution of Δ(C-STAT) values, the largest difference we found was 16.7, much smaller than the value of 40.5 for the actual data (see table 1). We therefore place a firm upper-limit on the probability that our fit of the exponential cutoff occurred by chance of 5×10^{-5}. This corresponds to a Gaussian equivalent significance of 4.05σ.

Our distribution of Δ(C-STAT) values shows a slight excess over the χ^2 distribution at large values indicating that perhaps the asymptotic distribution has not been reached for this number of trials. To be conservative, we do not evaluate the significance according to the conventional procedure of using the observed Δ(C-STAT) value of 40.5 and the χ^2 distribution. Unfortunately, the number of simulations that would be required to determine the significance of the observed cutoff is prohibitive. Nonetheless, the sizeable gap between the largest Δ(C-STAT) value obtained in the simulations, 16.7, and the observed value of 40.5 suggests that the significance is much larger than 4σ. For the 4 different sets of instrument response functions that we used in our study of the systematic uncertainties, we always found Δ(C-STAT)$\geq$ 32. The significance of the spectral cutoff will be hereafter quoted as $> 4\sigma$.

Using the fit results for the best model (Band+CUTPL), we estimate a fluence of $2.07 \pm 0.04 \times 10^{-4}\,{\rm erg\,cm^{-2}}$ (10 keV–10 GeV) from $T_0 + 3.3\,{\rm s}$ to $T_0 + 21.6\,{\rm s}$. These data

give an isotropic energy $\mathcal{E}_{\gamma,iso} = 2.24 \pm 0.04 \times 10^{54}$ erg, comparable to that of GRB 090902B (Abdo et al. 2009a).

We then performed a time-resolved spectral analysis of the prompt phase in the four time intervals *a, b, c, d*. The spectra are shown in figure 5, and the results are summarized in table 2, where the best-fit parameters are given for the statistically preferred model, and the C-STAT values are given for the various models. The extra power-law component is found to be very significant in intervals *c* and *d*, but not at the beginning of the prompt phase in intervals *a* and *b*. The spectral cutoff is significant at the $> 4\sigma$ level only in the common sharp peak (time interval *c*), where the GeV flux is the highest, but is only marginally significant ($\sim 4\sigma$) in time bin *d*.

In time interval *b*, the improvement in the fit statistics when adding the extra power-law component is only Δ(C-STAT) = 11.6. As a consequence, the parameters of the power-law are not very well constrained, yielding a normalization $B = 2.9^{+6.4}_{-1.0}\ 10^{-10}$ photons cm^{-2} s^{-1} keV^{-1} and a power-law index $\lambda = 1.7^{+0.2}_{-0.1}$. In time interval *c*, we found the cutoff energy to be $E_F = 0.40^{+0.13}_{-0.06}$ *stat.* $\pm\, 0.05$ *syst.* GeV (table 2). Note that we fixed the pivot energy at $E_{\rm piv} = 1$ MeV for time interval *c*, since this is the only interval where the extra power-law component is dominant over the Band component at very low energies, and setting $E_{\rm piv} = 1$ GeV resulted in very asymmetric and very large uncertainties, especially for the normalization *B* of the extra power-law component. We also tried to fit time interval *c* with a broken power-law model, see equation 2; but again the fit significance was close to that of the (Band+CUTPL) model, so that we cannot distinguish between the two models. The fit with a broken power law gave a break energy $E_{\rm break} = 264^{+233}_{-75}$ MeV and a photon index above $E_{\rm break}$ of $\lambda_h = -3.55^{+0.63}_{-3.28}$. In time interval *d*, the improvement in the fit statistics when adding a cutoff to the the extra power-law component is only 17.4 (roughly $\sim 4\sigma$), which is quite high, but not sufficient to claim the presence of an energy cutoff in this bin alone. However, as the cutoff is strong in the preceding time interval *c*, we looked at the behavior of the e-folding energy. For time interval *d*, the e-folding energy is found to be $E_F = 2.21^{+0.92}_{-0.69}$ GeV, which is much higher than the one found in interval *c* (the 2-σ confidence intervals for the cutoff in bins *c* and *d* actually exclude each other). This indicates a possible time evolution of the high energy cutoff.

4.2. LAT extended emission

As the burst was occulted by the Earth from $T_0 + 540$ s to $T_0 + 3000$ s, we performed the unbinned likelihood analysis using 'transient' class events in the time interval from $T_0 + 20$ s to $T_0 + 300$ s (a small margin is needed to safely define a circular ROI), and use 'diffuse'

class events after $T_0 + 3000\,\mathrm{s}$ [1]. 'Transient' class events are treated as in §4.1. In addition, for the 'diffuse' class events, we included in the model the standard galactic background component, described by the FITS model file `gll_iem_v02.fit`, with fixed normalization, and the standard isotropic background component, whose spectrum is given in the model file `isotropic_iem_v02.txt`, with the normalization left free. Both model files may be downloaded from the FSSC website.

We divided the LAT data into several time intervals, using intervals *a,b,c,d* for the prompt phase, and modeled the GRB extended emission spectrum as a power-law. For the period $T_0 + 3000\,\mathrm{s} - T_0 + 4800\,\mathrm{s}$, the fit resulted in a test statistic of 29.4, corresponding to a detection at a $\sim 5\sigma$ level, which is remarkable for a time period ~ 1 hour after the burst.

Figure 6 shows the flux and photon index versus time. The LAT flux follows a power-law with time-dependence $(T - T_0)^{-1.69\pm0.03}$ after $T_0 + 21.6\,\mathrm{s}$, similar to the behavior of bursts GRB 090510 and GRB 090902B (Abdo et al. 2009a,c; Ackermann et al. 2010a). Prior to $T_0 + 21.6\,\mathrm{s}$, the photon index varies significantly with values ranging from -2.5 to -1.7. By contrast, after $T_0 + 21.6\,\mathrm{s}$, the photon index is almost constant with values in the range -1.5 to -1.9. The soft spectral index in time interval c is consistent with the spectral break of the extra component described in section 4.1, and the gradual hardening from time bin d is consistent with its disappearance.

[1] See Atwood et al. (2009) for the definitions and recommended usage of the LAT event classes.

Table 1: Summary of GBM/LAT joint spectral fitting between $T_0 + 3.3\,\mathrm{s}$ and $T_0 + 21.6\,\mathrm{s}$. The flux range covered by both instruments is 10 keV–10 GeV.

Fitting model	Band	Band+PL	Band+CUTPL
Band function			
A (γ cm^{-2} s^{-1} keV^{-1})	0.176 ± 0.002	0.173 ± 0.003	$0.170\ ^{+0.001}_{-0.004}$
$E_{\rm peak}$ (keV)	249 ± 3	256 ± 4	$259\ ^{+8}_{-2}$
α (index 1)	−0.71± 0.01	−0.62± 0.03	$-0.64^{+0.02}_{-0.09}$
β (index 2)	−2.30± 0.01	$-2.59^{+0.04}_{-0.05}$	$-2.63^{+0.02}_{-0.12}$
Power-law			
B (10^{-10} γ cm^{-2} s^{-1} keV^{-1})	-	$3.17\ ^{+0.35}_{-0.33}$	$5.80\ ^{+0.81}_{-0.60}$
λ (index)	-	−1.79± 0.02	$-1.72^{+0.10}_{-0.02}$
$E_{\rm piv}$	-	1 GeV (fixed)	1 GeV (fixed)
High-energy cutoff			
E_F (GeV)	-	-	$1.41\ ^{+0.22}_{-0.42}$
Flux (γ cm^{-2} s^{-1})	42.2±0.1	43.5±0.3	43.3±0.2
Flux (10^{-5} erg cm^{-2} s^{-1})	1.18±0.01	1.15±0.02	1.13±0.02
C-STAT / DOF	1395.1 / 579	1287.8 / 577	1247.3 / 576
Δ(C-STAT)†	-	107.3	40.5

† *with respect to the preceding model (column).*

Table 2: Summary of GBM/LAT joint spectral fitting by best model in 4 time intervals. The flux range covered by both instruments is 10 keV–10 GeV.

Time interval from T_0 (s)	(a) 0.0–3.3	(b) 3.3–9.8	(c) 9.8–10.5	(d) 10.5–21.6
Prefered Model	Band	Band	Band+CUTPL	Band+PL
Band function				
A (γ cm^{-2} s^{-1} keV^{-1})	0.146 ± 0.004	0.302 ± 0.004	$0.335\ ^{+0.064}_{-0.012}$	0.100 ± 0.005
$E_{\rm peak}$	338 ± 10	288 ± 4	$209\ ^{+5}_{-16}$	186 ± 6
α (index 1)	-0.42 ± 0.03	-0.55 ± 0.01	$-0.59^{+0.39}_{-0.06}$	$-0.70^{+0.07}_{-0.06}$
β (index 2)	$-2.64^{+0.07}_{-0.09}$	-2.46 ± 0.02	$-3.69^{+1.81}_{-0.53}$	$-2.80^{+0.13}_{-0.18}$
Power-law				
B (10^{-10} γ cm^{-2} s^{-1} keV^{-1})	-	-	$7.56\ ^{\dagger}\ ^{+2.25}_{-0.50}$	$3.07\ ^{+0.38}_{-0.36}$
λ (index)	-	-	$-1.71^{+0.02}_{-0.05}$	-1.79 ± 0.03
$E_{\rm piv}$	-	-	1 MeV (fixed)	1 GeV (fixed)
High-energy cutoff				
E_F (GeV)	-	-	$0.40\ ^{+0.13}_{-0.06}$	-
Flux (γ cm^{-2} s^{-1})	31.4 ± 0.2	66.4 ± 0.3	109.0 ± 1.4	25.5 ± 0.2
Flux (10^{-6} erg cm^{-2} s^{-1})	9.96 ± 0.41	18.9 ± 0.30	29.22 ± 1.60	5.83 ± 0.30
C-STAT / DOF				
Band	622.4 / 579	944.2 / 579	655.9 / 579	1033.8 / 579
Band+PL	624.3 / 577	932.6 / 577	598.7 / 577	950.6 / 577
Band+CUTPL	618.8 / 576	928.3 / 576	574.2 / 576	933.2 / 576
Δ*(C-STAT)*				
Band$\rightarrow$(Band+PL)	-1.9	11.6	57.2	83.2
(Band+PL)$\rightarrow$(Band+CUTPL)	5.5	4.3	24.5	17.4

† *As* $\rm E_{piv}$ = 1 MeV, B *has the unit of* 10^{-4} γ cm^{-2} s^{-1} keV^{-1}

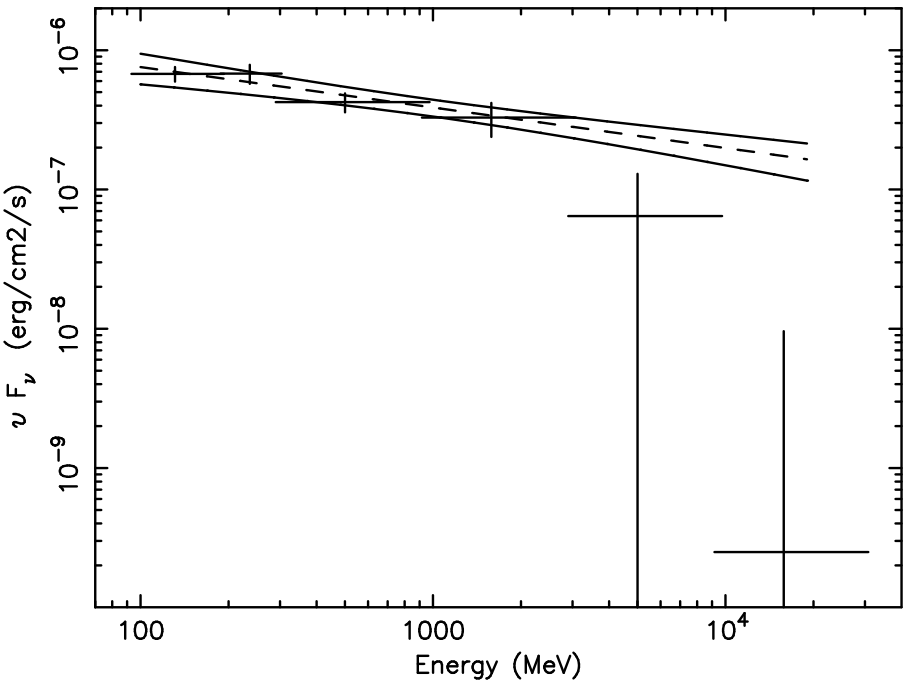

Fig. 3.— νF_ν spectrum of the data points from the LAT–only unbinned likelihood analysis of GRB 090926A between $T_0 + 3.3\,\mathrm{s}$ and $T_0 + 21.6\,\mathrm{s}$. Black dashed and solid lines show the best-fit power-law model and $\pm 1\ \sigma$ error contours, derived from the covariance matrix of the fit.

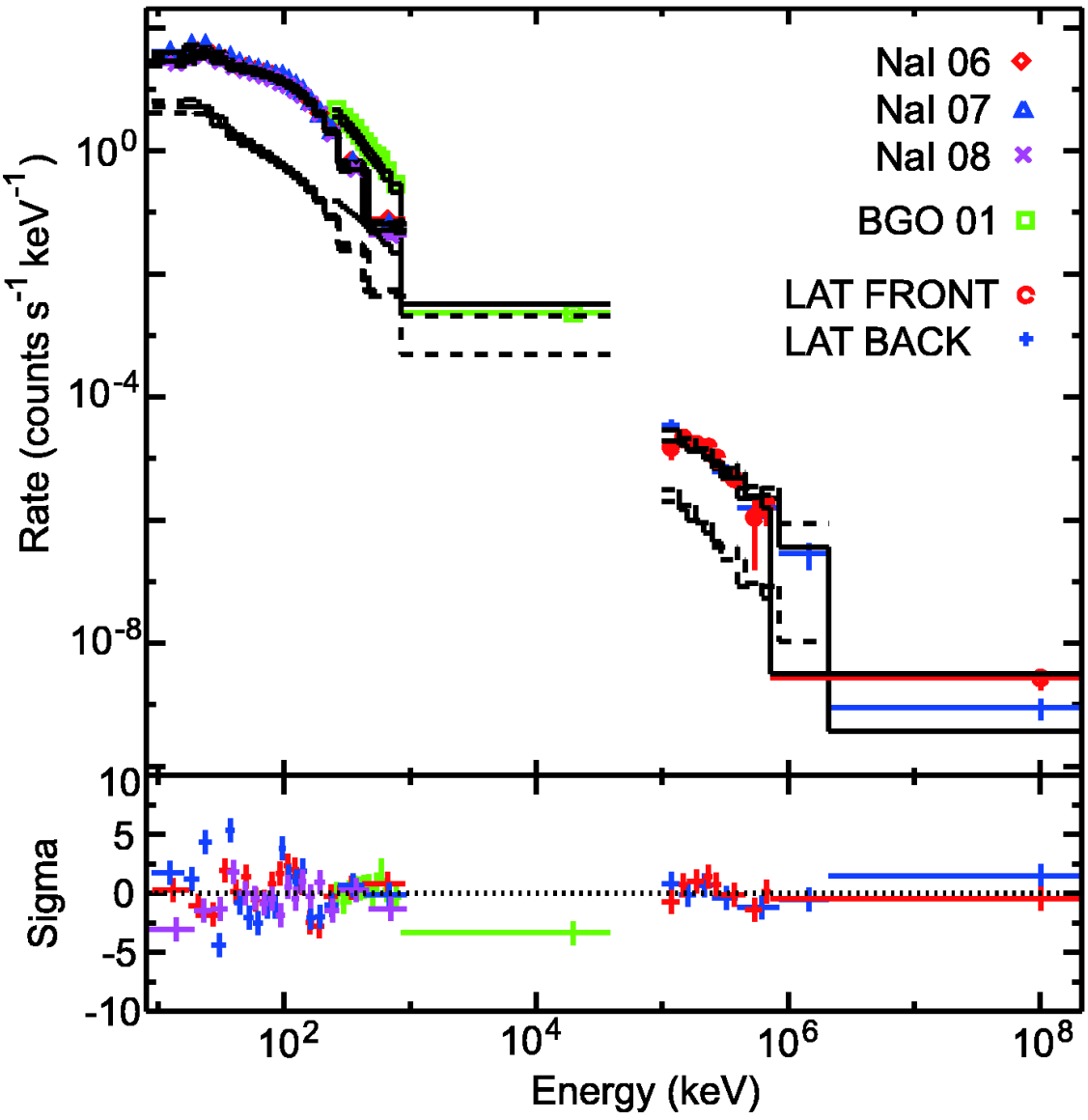

Fig. 4.— Joint spectral fitting of GBM and LAT data between $T_0 + 3.3\,\mathrm{s}$ and $T_0 + 21.6\,\mathrm{s}$. The top panel shows the count spectra and best-fit (Band+CUTPL) model (histograms). The lower panel shows the residual of the spectral fitting.

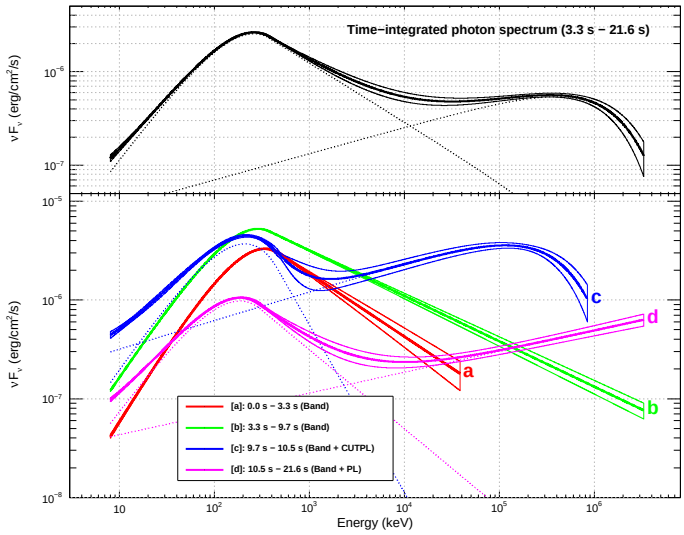

Fig. 5.— *Top*: The best-fit (Band+CUTPL) model for the time-integrated data plotted as a νF_ν spectrum. The two components are plotted separately as the dashed lines, and the sum is plotted as the heavy line. The ± 1 σ error contours derived from the errors on the fit parameters are also shown. *Bottom*: The νF_ν model spectra (and ± 1 σ error contours) plotted for each of the time bins considered in the time-resolved spectroscopy.

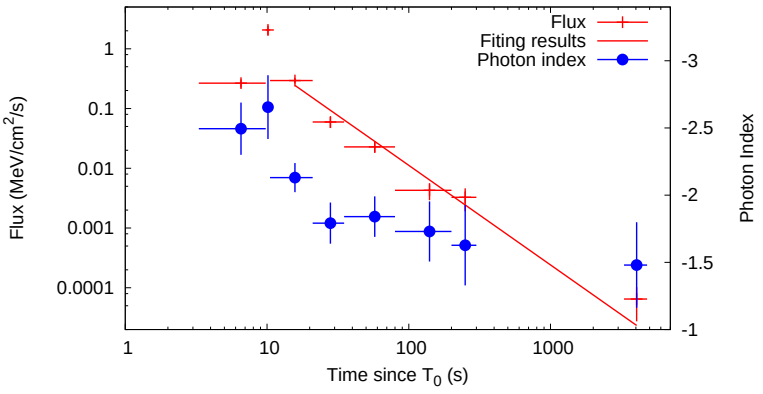

Fig. 6.— Time variation of the LAT flux (red cross) and photon index (blue filled circle) for the extended emission of GRB 090926A . After the end of the prompt emission at $T_0 + 21.6\,\mathrm{s}$, the flux decays following a power-law with index -1.69 ± 0.03 (red solid line).

5. Discussion and Interpretation

5.1. Prompt Emission Phase

The *Fermi* observations show that GRB 090926A clearly has an extra high-energy component in addition to the Band component in the time-integrated as well as in the time-resolved spectra. This is the third case of a LAT detection of an extra spectral component, after GRB 090510 and GRB 090902B (Ackermann et al. 2010a; Abdo et al. 2009a). That is, we have such detections in 3 out of the 4 brightest LAT GRBs (except GRB 080916C, see Abdo et al. 2009b). Since we require a confidence level of $> 5\sigma$ to claim a detection, we can unambiguously identify it only in the brightest LAT GRBs, which suggests that such a component may be intrinsically very common in GRBs.

The behavior in time interval c is remarkable, as the light curve shows a clear spike-like structure in the LAT energy range that is dominated by the extra spectral component. The spike in all the energy ranges has the peak times synchronized within 50 ms and shows similar pulse widths (see Figure 2), which indicates that the origins of the lowest and highest energy emission components as well as the Band component are related, i.e., they could either arise from the same physical region and possibly also the same spectral component, or are otherwise directly physically linked, such as photons generated in one emission region being scattered by electrons in the other emission region (see specific models discussed below).

The delayed onset of the LAT emission is common to almost all the LAT GRBs (except GRB 090217A, see Ackermann et al. 2010b). The delay may arise from the following four effects: (1) a flux increase of the Band component, (2) a hardening of the Band component (i.e., increase of the peak energy $E_{\rm peak}$ and/or high-energy spectral index β), (3) a flux increase of the extra component, or (4) an increase of the cutoff energy in the spectrum. However, effect (4) does not seem to be a major effect for LAT GRBs so far since there is no clear sign of a high-energy cutoff or steepening in the spectra before the LAT onsets (see also the discussion on GRB 080825C in Abdo et al. 2009d). The LAT detection of GRB 090926A starts from time interval b, and the clear emergence of the extra component occurs even later, ≈ 10 s after the onset of the Band component, so that this delay is likely to be due to the combination of (1) and (2). However, while no significant extra component is detected in time intervals a and b, it may still be present with a lower cutoff energy that falls under or close to the Band function model component, so that we may not exclude contributions from effects (3) or (4) to the delayed onset.

There are several theoretical models for the origin of the extra spectral component. The delayed extra component could be emitted from a forward shock that propagates into the external medium (Mészáros & Rees 1997; Sari et al. 1998), while the Band component

is thought to have a separate origin. The delay timescale of the extra spectral component would correspond to the time needed for the forward shock to sweep up material and brighten (Kumar & Barniol Duran 2009; Ghisellini et al. 2010; Razzaque 2010). The rapid variability observed in GRB 090926A is contrary to expectations from an external shock model, unless it is produced by emission from a small portion of the blast wave within the Doppler beaming cone. This could occur, for instance, if the external medium is clumpy on length scale $\approx \Gamma_f c \Delta T/(1+z) \simeq 10^{12}\ (\Gamma_f/10^3)(\Delta T/0.2\ \mathrm{s})$ cm, where Γ_f is the Lorentz factor of the forward shock and ΔT is the pulse duration (Dermer & Mitman 1999; Dermer 2008). This is based on interactions between a very thin shell, prior to the onset of the self-similar expansion phase, and an external medium with very small scale clumps. If the extra component is synchrotron emission from the forward shock, then the synchronization of the pulse peak times of the Band and extra component requires an explanation. One possibility is that the extra component arises from inverse Compton (IC) scattering of the radiation of the Band component by the high-energy electrons in the forward shock.

As for internal emission models, in which both spectral components arise within the ejecta, the extra component can be produced by IC scattering by energetic leptons or via hadronic processes. In either case, the time of the peak of the extra component would lag relative to the Band component in the same emission episode, although the time lag can be limited by a timescale comparable to the pulse duration, which would still be consistent with the observed synchronization of the two components. A simple leptonic model could comprise synchrotron plus synchrotron self-Compton (SSC) emission. Under the physical conditions typically assumed in the internal shock model (Rees & Mészáros 1994), all electrons emitting synchrotron emission cool on a timescale much shorter than the dynamical time (i.e., the electrons are in the fast cooling regime), so that the photon index α below $E_{\rm peak}$ should be -1.5, which is not consistent with the results from our fits, $-0.7 \lesssim \alpha \lesssim -0.4$. The synchrotron plus SSC model would need to overcome this problem. In the photospheric emission model of the Band component (e.g., Mészáros & Rees 2000), the extra component could be the IC of the photospheric emission by electrons in the dissipation region at large radius (Beloborodov 2009; Gao et al. 2009; Ryde et al. 2010). In this model, the low energy excess seen in interval c could be synchrotron emission of the electrons and the electron-positron pairs created by the cascade process, and the delay timescale of the extra component could be explained by the evolution of the jet physical conditions (Toma et al. 2010).

Hadronic processes, such as a photopion-induced pair cascade or proton/ion synchrotron emission (Asano et al. 2009; Razzaque et al. 2010; Wang et al. 2009) can make a spectral component that is distinct from that which is commonly observed during the prompt phase. Large values of the bulk Lorentz factor of the emitting region, $\Gamma \gtrsim 10^3$, imply large energy requirements for significant high-energy emission in either photo-hadronic or proton/ion

synchrotron models. The bulk Lorentz factor that is inferred by the argument of the pair absorption opacity for this burst, however, is relatively low ($\Gamma \sim 200$–700, see below). Thus for proton/ion synchrotron models, which require a heavily magnetically loaded shocked jet, the total energy requirements $\propto \Gamma^{16/3}$ (Wang et al. 2009; Razzaque et al. 2010) are smaller by a factor of ~ 7–5000 compared to the case of $\Gamma \sim 10^3$, much improving the viability of such models. The lower allowed values of Γ also reduce the energy requirements in photo-hadronic models, where non-thermal protons usually dominate the bulk energy (Asano et al. 2009; Wang et al. 2009; Ackermann et al. 2010a). Under the assumption that the photon field is homogeneous and steady in the emitting region, the efficiency of photo-hadronic interactions by high-energy protons at the peak of the Band spectrum component in this burst is estimated to be a few percent for $\Gamma \sim 10^3$. This efficiency scales as Γ^{-4}, which implies significant reduction of the total energy requirements for the lower allowed values of Γ. However, $\Gamma \lesssim 700$ is indicated under the assumption that the photon field is inhomogeneous and time-dependent, as will be discussed below, for which it is not so clear how the photo-hadronic interaction efficiency (as well as the neutrino production efficiency, see Murase & Nagataki (2006); Dermer et al. (2007); Razzaque (2009)) depends on Γ.

Another remarkable aspect of this burst is the spectral break (or cutoff) of the extra component that has been measured in the time-integrated spectrum of the prompt emission and for time interval c with a high significance ($> 4\,\sigma$; see sections 4.1, and tables 1, 2). This cutoff may be due to pair production ($\gamma\gamma \rightarrow e^+e^-$) within the emitting region, although we cannot rule out the possibility that there is an intrinsic spectral break related to the energy distribution of the emitting particles or the emission mechanism (e.g., IC scattering in the Klein-Nishina regime). Absorption by the extragalactic background light (EBL) cannot cause this spectral feature since the opacity at the observed break energy for the redshift of GRB 090926A is very small for practically all EBL models (Finke et al. 2010, and references therein). We focus on the spectral feature in time interval c to constrain the physical properties of the emitting region by introducing the critical photon energy E_c at which the pair production opacity is unity, $\tau_{\gamma\gamma}(E_c) = 1$ (e.g., Krolik & Pier 1991; Fenimore et al. 1993; Lithwick & Sari 2001).

In order to characterize the spectral break, we have fit the data with a model that consists of an extra power-law component modified by absorption due to pair production, but this spectral model is not unique. Although the instantaneous emission from a thin shell exhibits a photon spectrum like $f \propto E^{\lambda} \exp(-\tau_{\gamma\gamma}(E))$, the shape of the time-integrated spectrum of a single pulse may depend on the details of the emission mechanism (Baring 2006; Granot et al. 2008). For example, the simple model of an emitting slab leads to $f \propto E^{\lambda}[1 - \exp(-\tau_{\gamma\gamma}(E))]/\tau_{\gamma\gamma}(E)$, which is a smoothly broken power-law spectrum since $\tau_{\gamma\gamma}(E)$ is a power-law function of E when the intrinsic emission spectrum is a power-law function

(see below). A fully time-dependent and self-consistent semi-analytic calculation featuring emission from a very thin spherical shell over a finite range of radii (Granot et al. 2008) would also lead to a smooth break to a steeper power-law in the time-integrated spectrum of a single pulse. In section 4.2, we have fitted the observed extra spectral component for time interval c by two empirical functions: a power-law with exponential cutoff (Eq. 1) and a broken power-law model (Eq. 2). However, the photon counts are not enough to distinguish between the two models. In the time-dependent model of Granot et al. (2008), photons above the spectral break energy are expected to arrive predominantly near the onset of the spike. This signature may afford a more unambiguous indicator of the intrinsic opacity to pair production. Such an opportunity is also unavailable for GRB 090926A, however, due to insufficient photon counts above the spectral break. Here we only use the result of the former model (Eq. 1), and consider the e-folding energy E_F from the fit to be good approximation of E_c.

In order to derive the pair absorption function $\tau_{\gamma\gamma}(E)$, we first consider a simple model in which the photon field in the emitting region is uniform, isotropic, and time-independent in the comoving frame (see the supporting material for Abdo et al. 2009b). We assume that the opacity at the photon energy around E_c is dominated by the extra power-law component itself, instead of the Band component. This assumption is justified for the observed spectrum in time interval c, as shown below. Let us define the observed photon number spectrum of the extra component for one pulse, below the break energy, as $f(E) = f(E_{\rm piv})(E/E_{\rm piv})^{\lambda}$ in units of photons cm^{-2} keV^{-1}. The energy distribution of the photons in the comoving frame of the emitting region is written as

$$n'_{\gamma}(E') = \left(\frac{d_L}{R}\right)^2 \frac{\Gamma f(E_{\rm piv})}{(1+z)^3 W'} \left(\frac{E'}{E'_{\rm piv}}\right)^{\lambda}, \tag{3}$$

where the quantities with a prime are measured in the comoving frame, $d_L \simeq 5.17 \times 10^{28}$ cm is the luminosity distance of the source, and R, Γ, and W' are the distance from the central engine, the bulk Lorentz factor, and the comoving radial width of the emitting region, respectively. Photons with energy $E' = E'_c > m_e c^2$ annihilate mainly with target photons with energy $E'_{\rm ann} \sim 2m_e^2 c^4/E'_c$. Then the optical depth is of the order of $\tau_{\gamma\gamma}(E'_c) \sim 0.1\sigma_T E'_{\rm ann} n'_{\gamma}(E'_{\rm ann}) W'$, where the pair production cross section is approximated to be 0.1 times the Thomson cross section σ_T. More accurately, we have

$$\tau_{\gamma\gamma}(E'_c) = \sigma_T \left(\frac{d_L}{R}\right)^2 \frac{\Gamma E'_{\rm piv} f(E_{\rm piv})}{(1+z)^3} \left(\frac{E'_c E'_{\rm piv}}{m_e^2 c^4}\right)^{-\lambda-1} F(\lambda) = 1 \tag{4}$$

(Abdo et al. 2009b) where $F(\lambda) \approx 0.597(-\lambda)^{-2.30}$ for $-2.9 \leq \lambda \leq -1.0$. The relation $R \simeq \Gamma^2 c\Delta T/(1+z)$ is valid for a large class of emission mechanisms, where ΔT is the

variability time. Then we obtain

$$\Gamma \simeq \left[\sigma_T \left(\frac{d_L}{c\Delta T}\right)^2 E_{\rm piv} f(E_{\rm piv}) F(\lambda)(1+z)^{-2(\lambda+1)} \left(\frac{E_c E_{\rm piv}}{m_e^2 c^4}\right)^{-\lambda-1}\right]^{\frac{1}{2(1-\lambda)}}. \quad (5)$$

We can estimate Γ and R from the values of $E_{\rm piv}$, $f(E_{\rm piv})$, λ, and E_c, which are inferred from the observed spectrum. We have estimated the variability timescale of the Band component to be $\Delta T \simeq 0.15 \pm 0.01$ s from the analysis of the GBM emission in section 3. From the synchronization of the peak times and the similar pulse durations in all energy ranges, we may assume that the variability timescale of the extra component is the same. The power-law with exponential cutoff model with $E_{\rm piv} = 1$ MeV results in $B = 7.56^{+2.25}_{-0.50} \times 10^{-4}$ photons cm^{-2} keV^{-1}, $\lambda = -1.71^{+0.02}_{-0.05}$, and $E_c = E_F = 400^{+130}_{-60}$ MeV. We may estimate the normalization of the spectral fluence over the variability time ΔT around the spike by $f(E_{\rm piv}) \simeq 2B\Delta T$, where B is the normalization of the time-averaged spectral flux over interval c. Then we obtain $\Gamma \simeq 720 \pm 76$, where the error on Γ has been calculated by the statistical errors of the parameters λ, E_F, and ΔT as well as the error of $f(E_{\rm piv})$ taken as $\pm B\Delta T/2$. This error on Γ is much smaller than the uncertainty of Γ due to modeling the space inhomogeneity and the time dependence of the target photon field discussed below. The energy of the main target photons for the photons with E_c is $E_{\rm ann} \sim 2\Gamma^2 m_e^2 c^4/[(1+z)^2 E_c] \simeq 70\ (\Gamma/700)^2 (E_c/400\ {\rm MeV})^{-1}$ MeV, while the extra power-law component is dominant above ~ 1 MeV. Thus, our assumption that the target photons for the photons with energy E_c are from the extra component is justified. In this model, the emission radius is estimated to be $R \simeq \Gamma^2 c\Delta T/(1+z) \simeq 7 \times 10^{14}\ (\Gamma/700)^2 (\Delta T/0.15\ {\rm s})$ cm.

A fully time-dependent and self-consistent semi-analytic model by Granot et al. (2008) results in a significant reduction in $\tau_{\gamma\gamma}$ and in the inferred value of Γ by a factor of ~ 3 compared to simpler models like the above calculation, i.e., $\Gamma \simeq 220$ for this burst. Under the typical physical conditions for the shock emitting the bright γ-rays, electrons are in the fast cooling regime, so that most of the radiation is emitted within a very thin layer behind the expanding shock front (e.g., Granot et al. 2000). The reduction in $\tau_{\gamma\gamma}$ occurs mainly since the high-energy photons are emitted from a very thin cooling layer, so that those that are emitted from angles $< 1/\Gamma$ relative to the line of sight immediately propagate ahead of the shock front, and can therefore potentially pair produce only with photons that propagate at fairly small angles, θ_{12}, relative to their own direction. The small values of θ_{12} suppress the interaction rate ($\tau_{\gamma\gamma} \propto 1 - \cos\theta_{12}$), and increase the threshold energy for pair production, $E_1 E_2 (1+z)^2 > 2(m_e c^2)^2/(1-\cos\theta_{12})$, where E_1 and E_2 are measured at Earth. The time dependence also reduces the time-averaged opacity over a single spike in the light curve, since the opacity is initially very low and gradually increases as the photon field builds-up, approaching its quasi-steady state value on the dynamical time (by which time

the emission episode leading to the spike in the light curve is typically over). Furthermore, in this model both the photon density and the typical value of θ_{12} decrease with radius along the trajectory of a test photon, further reducing $\tau_{\gamma\gamma}$. For our discussion below we adopt the value of $\Gamma \sim 200$–700, intermediate between the values inferred by the previous simple model and the time-dependent model for a very thin cooling layer. The motivation for this is that in some of the models discussed above the high-energy photons are expected to be emitted from the bulk of the shocked region, rather than from a thin cooling layer behind the shock front, in which case such an intermediate value of the opacity might be expected.

The spectrum for time interval *d* also has an extra power-law component. It is much dimmer than that for time interval *c*, but its spectral index is similar. The break feature is marginally significant. A straightforward interpretation of this behavior is that the critical energy E_c is larger than that for interval *c*. However, it is also possible that a different emission component, which is responsible for the LAT temporally extended emission at $T \gtrsim 20$ s, contributes to the high-energy emission in interval *d*. This may hide a possible spectral break of the extra component.

We emphasize that this burst is the first GRB that exhibits a spectral break that can be used to estimate (as opposed to bound) its bulk Lorentz factor, presuming that this feature is due to pair production attenuation. Other LAT GRBs do not show any clear high-energy spectral breaks (a circumstance evinced in EGRET bursts with lower count statistics; see the overview in Baring 2006). The lower limits of the bulk Lorentz factors for those GRBs have been derived by $\tau_{\gamma\gamma}(E_h) < 1$, where E_h is the highest photon energy detected; $\Gamma \gtrsim 900, \Gamma \gtrsim 1200$, and $\Gamma \gtrsim 1000$, for GRB 080916C, GRB 090510 and GRB 090902B, respectively, using the simple model described above. In the time-dependent thin-shell model of Granot et al. (2008) all of these lower limits would be lower by about a factor of ~ 3. Thus, the inferred $\Gamma \sim 200$–700 of GRB 090926A is smaller than the lower limits for other LAT GRBs. On the other hand, it is consistent with the constraints on Γ for other GRBs put by different methods: the observed broad flux peaks of some optical afterglows, typically $\sim 10^2$–10^3 s after the burst triggers, appear to signify the afterglow onset, and thus indicate $\Gamma \sim$ a few $\times$ 100 (Molinari et al. 2007; Oates et al. 2009); the possible thermal emission in some bursts may suggest the photospheric radii of the jets, which indicate $\Gamma \simeq 300$–700 (Pe'er et al. 2007; Ryde et al. 2010). These suggest that the Lorentz factors of GRBs are widely distributed over a range $\gtrsim 10^2$.

5.2. Temporally Extended Emission

The emission in the LAT energy range lasts much longer than that in the GBM energy range, and the flux in the LAT energy range shows a power-law decay, $F_\nu \propto (T - T_0)^a$ with $a = -1.69 \pm 0.03$. This behavior is similar to that seen in other LAT GRBs, which have decay indices $a = -1.2 \pm 0.2$ for GRB 080916C (Abdo et al. 2009b), $a = -1.38 \pm 0.07$ for GRB 090510 (De Pasquale et al. 2010), and $a \approx -1.5$ for GRB 090902B (Abdo et al. 2009a). These may be explained as synchrotron emission from the external forward shock (Kumar & Barniol Duran 2009; Ghisellini et al. 2010; De Pasquale et al. 2010).

For GRB 090926A, this interpretation seems consistent with the nearly constant spectral index at $\gtrsim 20$ s (Figure 6). In this scenario, the starting time of the self-similar phase of the forward shock should be $\lesssim T_{\rm dur} \simeq 13$ s. This means that the ejecta is in the thick shell regime or in the borderline of the thick and thin shell regimes (Sari 1997; Kobayashi & Zhang 2003), which corresponds to $T_{\rm dec} = [(3-k)\mathcal{E}_{k,iso}/(2^{5-k}\pi A_{\rm ext} c^{5-k}\Gamma^{2(4-k)})]^{1/(3-k)}(1+z) \lesssim T_{\rm dur} \simeq 13$ s, where $\mathcal{E}_{k,iso}$ is the isotropic-equivalent kinetic energy of the ejecta producing the external shock, and the external density profile is defined as $n_{\rm ext} m_p = A_{\rm ext} R^{-k}$. This relation allows us to put a lower limit on the initial Lorentz factor of the ejecta. For the uniform density case ($k = 0$), $\Gamma \gtrsim 750\ (\mathcal{E}_{\gamma,iso}/2 \times 10^{54}\ {\rm erg})^{1/8}(\eta_\gamma/0.2)^{-1/8}(n_{\rm ext}/1\ {\rm cm}^{-3})^{-1/8}$, and for the wind medium case ($k = 2$), $\Gamma \gtrsim 290\ (\mathcal{E}_{\gamma,iso}/2 \times 10^{54}\ {\rm erg})^{1/4}(\eta_\gamma/0.2)^{-1/4}(A_{\rm ext}/5 \times 10^{11}\ {\rm g\ cm}^{-1})^{-1/4}$, where we define $\eta_\gamma = \mathcal{E}_{\gamma,iso}/\mathcal{E}_{k,iso}$, and $A_{\rm ext} \simeq 5 \times 10^{11}$ g cm^{-1} corresponds to the value of typical Wolf-Rayet stars in our Galaxy, which have mass loss rates $\simeq 10^{-5} M_\odot$ yr^{-1} and wind velocities $\simeq 1000$ km s^{-1}. Cenko et al. (2010) analyzed the observed late optical and X-ray afterglows of GRB 090926A and showed that they can be explained by synchrotron emission from the adiabatic forward shock propagating into the wind medium with $A_{\rm ext} \simeq 3.4 \times 10^{11}$ g cm^{-1}. This could provide $\Gamma \gtrsim 320\ (\eta_\gamma/0.2)^{-1/4}$, which may be consistent with $\Gamma \sim 200$–700 of this burst inferred by the pair attenuation opacity argument. Note that the estimate $\Gamma \sim 200$–700 is only for the bulk Lorentz factor of the shell emitting the spike in time interval c, while the lower limit $\Gamma \gtrsim 320(\eta_\gamma/0.2)^{-1/4}$ is relevant for the mean or typical value, weighed over the energy in the whole outflow.

6. Conclusions

GRB 090926A is one of the brightest long bursts detected by the GBM and LAT instruments on *Fermi* with high energy events up to ~ 20 GeV. As in other bursts (GRB 090510, GRB 090902B), this burst shows an extra hard component in its integrated spectrum, but for the first time we significantly detect a spectral break around 1.4 GeV. The time-resolved spectral analysis shows that the extra component significantly dominates the emission in

the high (> 1 MeV) energy range at the time of the narrow pulse which is simultaneously observed by LAT and GBM. At earlier times, the spectrum is described by a standard Band model while at later times the extra component is significant, but a spectral break feature is only marginally significant. Correlation between the lowest and highest energy light curves implies that the origins of the Band component and the extra power-law component are related around the time of the sharp pulse.

The ~ 3.3 s delay of the LAT emission onset can be explained as the overall flux increase and the spectral hardening of the Band component, since the clear emergence of the extra component occurs only at a later time. However we may not exclude a contribution from the extra component in the early times, whose flux is intrinsically just below the Band component or suppressed by a lower spectral cut-off. The high temporal variability of the extra component and the correlation of the Band and extra components put strong constraints on the external shock scenario: the external medium needs to be highly clumpy, and the emission mechanisms of the two components should be related.

From the spectral break we have computed the bulk Lorentz factor of the emitting shell and find a range of $\Gamma \sim 200$–700, depending on the assumption of the homogeneity and time-dependence of the photon field, as well as on the assumption that the cutoff is due to the pair production attenuation. Even if we cannot distinguish between leptonic and hadronic emission for the extra component, we note that such a moderate Lorentz factor could alleviate the problem of the energy budget in hadronic emission models, as for GRB 090510. Comparison of this estimate with the large lower limits for other LAT GRBs and the estimates for GRBs that occurred before *Fermi* may imply that the bulk Lorentz factors of GRBs are widely distributed over a range of values $\gtrsim 100$. In addition, the early deceleration of the forward shock inferred by the LAT temporal extended emission and the density of the external medium inferred by the late optical and X-ray afterglows (Cenko et al. 2010) can put a lower limit on the bulk Lorentz factor of the entire shell just before the deceleration, $\Gamma \gtrsim 290(\eta_\gamma/0.2)^{-1/4}$, which is consistent with the estimate of $\Gamma \sim 200$–700 for the region that corresponds to the emission around the spike.

Further LAT detections of bright GRBs will enable us to observe other bright extra components and constrain their origins and spectral breaks and their relation to excesses below 20 keV and the temporally extended emission.

We thank R. Mochkovitch for useful discussions. The *Fermi* GBM collaboration acknowledges support for GBM development, operations and data analysis from NASA in the US and BMWi/DLR in Germany. The *Fermi* LAT Collaboration acknowledges support from a number of agencies and institutes for both development and the operation of the

LAT as well as scientific data analysis. These include NASA and DOE in the United States, CEA/Irfu and IN2P3/CNRS in France, ASI and INFN in Italy, MEXT, KEK, and JAXA in Japan, and the K. A. Wallenberg Foundation, the Swedish Research Council and the National Space Board in Sweden. Additional support from INAF in Italy and CNES in France for science analysis during the operations phase is also gratefully acknowledged.

REFERENCES

Abdo, A. A., et al. 2009a, ApJ, 706, L138 (GRB 090902B)

Abdo, A. A., et. al. 2009b, Science, 323, 1688 (GRB 080916C)

Abdo, A. A., et al. 2009c, Nature, 462, 331 (GRB 090510)

Abdo, A. A., et al. 2009d, ApJ, 707, 580 (GRB 080825C)

Abdo, A. A., et al. 2010, ApJ, 712, 558 (GRB 081024B)

Ackermann, M., et al. 2010a, ApJ, 716, 1178 (GRB 090510)

Ackermann, M., et al. 2010b, ApJ, 717, L127 (GRB 090217A)

Asano, K., Guiriec, S., & Mészáros, P. 2009a, ApJ, 705, L191

Atwood, W. B., et al. 2009, ApJ, 697, 1071

Band, D. L., et al., 1993, ApJ, 413, 281

Band, D. L., et al., 2009, ApJ, 701, 1673

Baring, M. G. 2006, ApJ, 650, 1004

Beloborodov, A. M. 2009, MNRAS in press (arXiv:0907.0732)

Bissaldi, E. 2009, GRB Coordinates Network, 9933, 1

Cash, W., 1979, ApJ, 228, 939

Cenko, S. B. 2010 submitted to ApJ(arXiv:1004.2900)

De Pasquale, M., et al. 2010, ApJ, 709, L146

Dermer, C. D. 2008, ApJ, 684, 430

Dermer, C. D., & Mitman, K. E. 1999, ApJ, 513, L5

Dermer C. D., Ramirez-Ruiz, E., & Le, T. 2007, ApJ, 664, L67

Dorman B., Arnaud K. A. & Gordon C. A., 2003, BAAS, Vol. 35, p.641

Falcone, A., D., et al. 2008, (arXiv:0810.0520)

Fan, Y. Z., & Piran, T. 2008, Frontiers of Physics in China, 3, 306

Fenimore, E. E., Epstein, R. I., & Ho, C. 1993, A&AS, 97, 59

Finke, J. D., Razzaque, S., & Dermer, C. D. 2010, ApJ, 712, 238

Gao, W. H., Mao, J. R., Xu, D., & Fan, Y. Z. 2009, ApJ, 706, L33

Ghisellini, G., Ghirlanda, G., Nava, L., & Celloti, A. 2010, MNRAS, 403, 926

Granot, J., Cohen-Tanugi, J., & do Couto e Silva, E. 2008, ApJ, 677, 92

Granot, J., Piran, T., & Sari, R. 2000, ApJ, 534, L163

Kaneko, Y., et al. 2006, ApJS, 166, 298

Kobayashi, S., & Zhang, B. 2003, ApJ, 597, 455

Kouveliotou, C., et al. 1993, ApJ, 413, L101

Krolik, J. H., & Pier, E. A. 1991, ApJ, 373, 277

Kumar, P., & Barniol Duran, R. 2009, MNRAS, 400, L75

Lithwick, Y., & Sari, R. 2001, ApJ, 555, 540

Malesani, D., et al. 2009, GRB Coordinates Network, 9942, 1

Meegan, C., et al. 2009, ApJ, 702, 791

Mészáros, P. 2006, Reports on Progress in Physics, 69, 2259

Mészáros, P., & Rees, M. J. 1997, ApJ, 476, 232

Mészáros, P., & Rees, M. J. 2000, ApJ, 530, 292

Molinari, E., et al. 2007, A&A, 469, L13

Murase, K., & Nagataki, S. 2006, PRD, 73, 063002

Noda, K., et al. 2009, GRB Coordinates Network, 9951, 1

Norris, J. P. and Nemiroff, R. J. and Bonnell, J. T. and Scargle, J. D. and Kouveliotou, C. and Paciesas, W. S. and Meegan, C. A. and Fishman, G. J. 1996, ApJ, 459, 393

Oates, S. R., et al. 2009, MNRAS, 395, 490

Pe'er, A., et al. 2007, ApJ, 664, L1

Razzaque, S., Dermer, C. D., Finke, J. D., & Atoyan, A. 2009, AIP Conf. Proc., 1133, 328

Razzaque, S. 2010, Astrophys. J. Lett. 724, L109-L112

Razzaque, S., Dermer, C. D., & Finke, J. D. 2010, Open Astron. J. 3, 150-155

Razzaque, S., Mészáros, P., & Zhang, B. 2004, ApJ, 613, 1072

Rees, M. J., & Mészáros, P. 1994, ApJ, 430, L93

Ryde, F., et al. 2010, ApJ, 709, L172

Sari, R. 1997, ApJ, 489, L37

Sari, R., Piran, T., & Narayan, R. 1998, ApJ, 497, L17

Toma, K., Wu, X. F., & Mészáros, P. 2010, (arXiv:1002.2634)

Uehara, T., Takahashi, H., & McEnery, J. 2009, GRB Coordinates Network, 9934, 1

Vetere, L., Evans, P., & Goad, M. 2009, GRB Coordinates Network, 9936, 1

Wang, X. Y., Li, Z., Dai, Z. G., & Mészáros, P. 2009, ApJ, 698, L98

Zhang, B. 2007, Chinese Journal of Astronomy and Astrophysics, 7, 1